Forside

Eksamensinformation
NFYB05035E - Bachelorprojekt i de fysiske fag, Niels Bohr Institutet - ID:jdp286 (Asbjørn Frede Lyngholm Preuss)

Besvarelsen afleveres af
Asbjørn Frede Lyngholm Preuss
jdp286@alumni.ku.dk

Eksamensadministratorer
Eksamensteam, tel 35 33 64 57
eksamen@science.ku.dk

Bedømmere
Kim Lefmann
Eksaminator
lefmann@nbi.ku.dk

Niels Bech Christensen
Censor
nbch@fysik.dtu.dk

Besvarelsesinformationer

Titel: Extended critical range in Bi2Fe4O9: An investigation of the interesting inelastics of frustrated magnets
Titel, engelsk: Extended critical range in Bi2Fe4O9: An investigation of the interesting inelastics of frustrated magnets
Tro og love-erklæring: Ja

Extended critical range in $Bi_2Fe_4O_9$

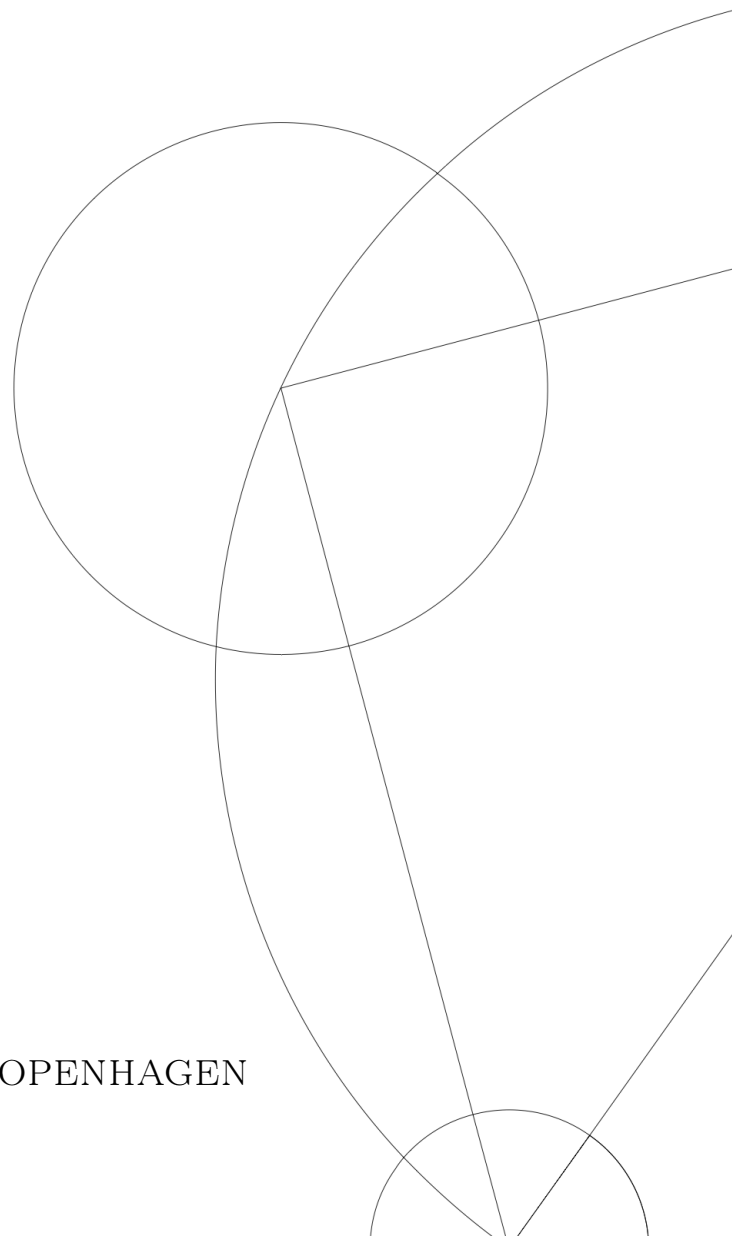An investigation of the interesting inelastics of frustrated magnets

Bachelor Project
Written by *Asbjørn F. L. Preuss*
June 16, 2023

Supervised by
Kim Lefmann

University of Copenhagen

NAME OF INSTITUTE:	Niels Bohr Institute
NAME OF DEPARTMENT:	X-ray and Neutron Science
AUTHOR(S):	Asbjørn F. L. Preuss
EMAIL:	asbjoern.preuss@nbi.ku.dk
TITLE AND SUBTITLE:	Extended critical range in $Bi_2Fe_4O_9$ - An investigation of the interesting inelastics of frustrated magnets
SUPERVISOR(S):	Kim Lefmann
HANDED IN:	16. Jun. 2023
DEFENDED:	04. Jul. 2023

NAME _____

SIGNATURE _____

DATE _____

Abstract

The range of magnetic scattering in $Bi_2Fe_4O_9$ has been investigated through elastic and inelastic neutron scattering on a $2.35\,g$ single crystal at the CAMEA neutron spectrometer, PSI. The magnetic scattering was measured at temperatures more than $100\,K$ away from the critical temperature, which is where the system should disorder and magnetic scattering stop. The temperature dependence of the integrated diffuse intensity was fitted using critical exponents revealing different fitted critical temperatures depending on whether $T > T_N$, or $T < T_N$, $(73 \pm 4)\,K$ and $(296 \pm 5)\,K$ respectively.

Furthermore, an unexpected shift of the magnetic scattering signal in reciprocal space was detected showing that there is still much to learn about this system.

Acknowledgements

Contents

1 Introduction

Magnets have been a part of the human experience since ancient China where lodestones where used to detect iron. This was believed to be due to compatible chi between these two materials [1]. Many different theories have since been tried to describe magnets, but it wasn't until 1820 that Ørsted noticed a connection between electricity and magnetism. This was further investigated by Ampere and finally, classically collected as part of Maxwell's four equations in the late 19th century [10].

Magnetic interactions in crystals lead to a variety of possibilities regarding how the quantum mechanical spins should align in order to minimise the energy of the system. For ferromagnets the spins align and for antiferromagnets the spins antialign [5]. The latter can lead to degeneracy of the ground state, since the spins might need to antialign to several spins that are themselves antialigned. This degeneracy is known as frustration [16].

The field of frustrated systems is still new and not well understood. Recently it was measured in the frustrated system h-YMnO$_3$ that the critical scattering spans a temperature range much larger than expected for ordinary magnetic systems [13]. In order to see if this is a general feature of frustrated magnetic systems or unique to h-YMnO$_3$, this project has aimed to investigate the magnetic scattering of neutrons in Bi$_2$Fe$_4$O$_9$.

Bi$_2$Fe$_4$O$_9$ is an interesting example of a frustrated system, as it has an (almost) Cairo-pentagonal structure [3]. The measurements in this thesis were done on CAMEA, a neutron spectrometer at the Paul Scherrer Institut in Switzerland, leading to a high data resolution and making new discoveries possible.

2 Magnetism

2.1 Interactions between particles and fields

Important to the topic of neutron scattering is the field of a magnetic dipole as it constitutes the interactions accountable for magnetic scattering. A magnetic dipole is classically thought of as an electron moving in a small orbit creating a current and thus a magnetic field [10]. The strength of such a dipole is known as its magnetic moment, $\boldsymbol{\mu}$. A magnetic dipole placed at origin creates a vector potential according to [10]

$$\boldsymbol{A}\left(\boldsymbol{r}\right) = \frac{\mu_0}{4\pi}\frac{\boldsymbol{\mu}\times\boldsymbol{r}}{r^2},\tag{1}$$

which in return leads to a magnetic field

$$B\left(\boldsymbol{r}\right) = \boldsymbol{\nabla}\times\boldsymbol{A} = \frac{\mu_0}{4\pi}\boldsymbol{\nabla}\times\left(\frac{\boldsymbol{\mu}\times\boldsymbol{r}}{r^2}\right).\tag{2}$$

Magnetic fields interact with atoms with a strength proportional to the magnetic moment of the atom. This is known as the Zeeman effect [11]. The strength of the Zeeman potential is given by

$$H_Z = -\boldsymbol{\mu}\cdot\boldsymbol{B}.\tag{3}$$

Though we classically think of the magnetic moment as a charged ball in some orbit, it is in quantum mechanics instead proportional to the spin of the particles and can for some be found in data sheets and books.

2.2 Crystals

When dealing with crystals, it is essential to consider not only the scattering effects of magnetism, but also how magnetism might affect the structure of the crystal.

If we place an atom with spin s_j at each lattice point in a one-dimensional lattice we might get a constellation as depicted in Figure 1.

Figure 1: Spins in a 1D lattice

The Hamiltonian of any two electrons can be described by their combined state, which for reasons of symmetry is either the singlet or the triplet state [5],

$$\Psi_S = \frac{1}{\sqrt{2}} \left[\psi_a(\boldsymbol{r}_1) \psi_b(\boldsymbol{r}_2) + \psi_a(\boldsymbol{r}_2) \psi_b(\boldsymbol{r}_1) \right] \chi_S \tag{4}$$

$$\Psi_T = \frac{1}{\sqrt{2}} \left[\psi_a(\boldsymbol{r}_1) \psi_b(\boldsymbol{r}_2) - \psi_a(\boldsymbol{r}_2) \psi_b(\boldsymbol{r}_1) \right] \chi_T. \tag{5}$$

The spacial part is denoted with ψ and the spin part with χ. By subtracting the energies, $\langle \Psi_k | H | \Psi_k \rangle$, from each other, we get the spin-dependent part of the Hamiltonian as

$$H_{spin} = -2 \cdot \frac{E_S - E_T}{2} \boldsymbol{S}_1 \cdot \boldsymbol{S}_2. \tag{6}$$

The fraction in front is known as the exchange factor[1], J_{12}. From here the general system can be described by summing over all these interactions in a Hamiltonian known as the Heisenberg Hamiltonian [5],

$$H_{heis.} = -2 \sum_{i>j} J_{ij} \boldsymbol{S}_i \cdot \boldsymbol{S}_j. \tag{7}$$

Depending on the exchange factor, the Hamiltonian minimises the energy either when the neighbouring spins are aligned or antialigned. Thus, we can characterise the magnets as those having $J > 0$, ferromagnets; and $J < 0$, anti-ferromagnets.

The Hamiltonian can be further simplified, when crystals contain anisotropies. In such a case the spins are no longer free to orient in all possible directions. Limited this way, some of the degrees of freedoms are removed and in the most extreme case the spins are restricted to be either up or down. This is known as the Ising Hamiltonian [5].

It is important to note that the magnetic unit cell in the antiferromagnetic case no longer is the same size as the crystal unit cell, as the alternating spins only repeat at every other lattice point.

The exchange interaction is only applicable, when two electrons are close enough to each other to be in a combined state that need to be treated as such. If an oxygen atom

---

[1]Though some use $E_S - E_T$ [5], and some swap the places of E_S and E_T in the expression [3].

is placed between a two transition metals, such as iron, it can act as a bridge between the two, allowing interactions on larger scales. This process is known as superexchange and works by aligning the electrons in the one metal atom with one electron in the oxygen orbital and aligning the other electron with an electron in the other transition metal. This leads to a setup where antiferromagnetic behaviour is often energetically favoured since the two oxygen electrons need to be of different spin due to the Pauli exclusion principle and thus locks one electron in place, in the ferromagnetic case [5].

2.3 Magnetic order

As the Heisenberg Hamiltonian is time-independent we can use it to find the ground state, which the system must be in at zero temperature. For ferromagnets this is when the spins align, and for antiferromagnets it is when they anti-align (See Figure 2).

At zero temperature the system is said to be ordered, and it will stay like this as we heat it up until it starts "melting". At some high temperature all order is lost, and we have transitioned into another phase. This leads us to define some order parameter which shows when this transition happens. For an antiferromagnet this could be the difference in the magnetisation of the sublattice with all spins aligned upwards, M_+, and the magnetisation of the sublattice consisting of spin-down atoms, M_-. When the lattice is ordered the sublattice magnetisations should be equal in magnitude, $|M_-| = |M_+| = M$, so the difference is $2M$. When the order ceases to exist, each sublattice will on average have a magnetisation of 0, and thus the order parameter is zero itself. These order parameters, p, can be defined for different phase transitions, but always with $p \neq 0$ for $T < T_C$ and $p = 0$ for $T > T_C$, where T_C is the critical temperature of the phase transition.

2.3.1 Frustrated magnetism

The minimisation of the energy in the different models is all well and good in the case of one dimensional lattices, as the one in Figure 1 on the previous page or even for two-dimensional square lattices as the two leftmost on Figure 2. Problems arise in less trivial structures, where anti-alignment is favoured. Most famously geometric frustration is found in the triangular lattice.
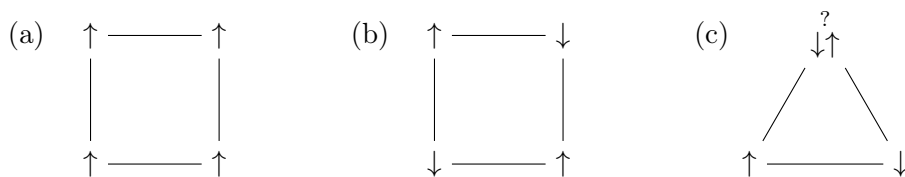
Figure 2: Examples of magnetic order. (a) Ferromagnetic order. All of the spins align. (b) Antiferromagnetic order, where all adjacent spins antialign. (c) The upper spin in this system has no clear way to antialign with both of the closest neighbours. Thus the system is said to be frustrated. This is known as geometric frustration.

The upper spin in Figure 2c is trying to both align upwards and downwards to be antialigned to both of the lower spins, in the case of the Ising Hamiltonian. This is of course not possible, so the system has to "choose" one of the two. This is known as

magnetic frustration. In the case of the triangular lattice in Figure 2 the ground state has a six-fold degeneracy; each corner has two possibilities of equal energy when the other spins are fixed. For larger systems, this degeneracy turns macroscopic leading to new interesting phenomena [16].

2.3.2   Magnons

At temperatures above absolute zero the order can be disrupted by thermal excitations of the lattice. These vibrations can be quantised as phonons [5]. The same is true for the magnetic order, where the spin of one atom affects the magnetic field of the neighbouring atoms. These in return moves and we see a wave in much the same way as with the phonons but for the spins instead of the lattice. This is possible since the cost of producing a spin wave is vanishingly small, so even small thermal excitations are enough. Such excitations are called Goldstone modes, and the quantisation of this specific type of excitations are known as magnons [5].

3   Magnetism in $Bi_2Fe_4O_9$

$Bi_2Fe_4O_9$ is an orthorombic crystal with sidelengths $a = 7.9\,\text{Å}, b = 8.4\,\text{Å}$, and $c = 6.0\,\text{Å}$ [8]. The placement of the Fe atoms, $S = \frac{5}{2}$, and O atoms, which are the relevant ones for magnetism, are shown in Figure 3. The Fe atoms are placed in an almost Cairo pentagonal lattice with some of the atoms paired just above and just below the pentagonal plane. The magnetic interactions in bismuth ferrite are due to the eight iron atoms in the unit cell interacting with each other through superexchange [3]. The interactions can be seen visualised in Figure 3. $Bi_2Fe_4O_9$ shows long range magnetic order at temperatures below $T_N \sim 240\,\text{K}$ [3], as seen in Figure 4. From this order it is possible to identify the magnetic order vector $\boldsymbol{Q}_m = \left(\frac{1}{2}, \frac{1}{2}, \frac{1}{2}\right)$. We thus expect magnetic peaks at half-integer coordinates in reciprocal space.

Table 1: Values for the five different exchange factors at play in $Bi_2Fe_4O_9$. Note that Le et al. [19] and Beauvois et al. [3] disagree significantly on J_1. The potential ferromagnetic interaction is not severe enough to change the degree of frustration in the system.

	J_1	J_2	J_3	J_4	J_5
[meV], [3]	(-3.7 ± 0.2)	(-1.3 ± 0.2)	(-6.3 ± 0.2)	(-24.0 ± 0.8)	(-2.9 ± 0.1)
[meV], [19]	(0.22 ± 0.03)	(-1.39 ± 0.05)	(-6.5 ± 0.2)	(-27.6 ± 0.6)	(-3.1 ± 0.2)

The fact that most, or maybe even all, of these interactions have $J < 0$, meaning that they are antiferromagnets, combined with the almost Cairo pentagonal lattice leads to a frustrated system. Especially since both sources [3, 19] agree on $J_{3-5} < 0$. These are the in-plane interactions and in themselves, they lead to geometric frustration. Worth noting is the difference between J_3 and J_5. Even though the distances between the iron atoms are the same, the exchange factors are significantly different. This is due to the different constellations of oxygen atoms and thus different strengths of the superexchanges.
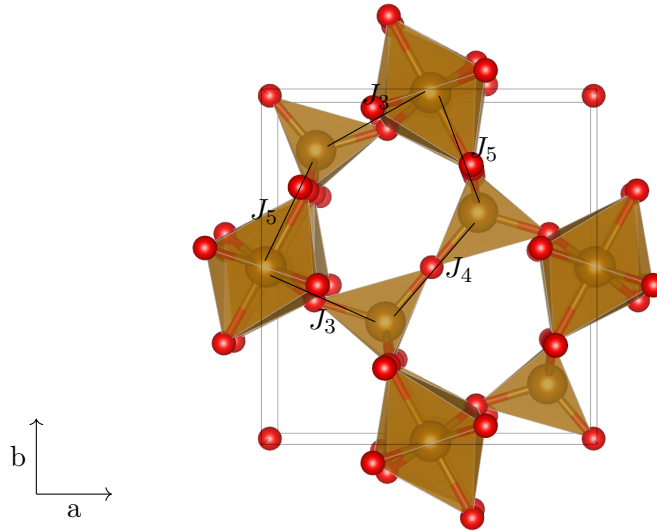
Figure 3: Structure of the unit cell in bismuth ferrite. Fe atoms are shown in golden brown and O atoms in red. Bismuth atoms are not shown due to their non-magnetic behaviour. The magnitude of the different exchange factors can be seen in Table 1. The illustration is made using VESTA [21]. Positions of the atoms were obtained from Da Silva et al. [8]. The interaction J_1 is between the pairs of Fe ions sandwiching the pentagonal plane and J_2 is between the same Fe ions but in-between planes.
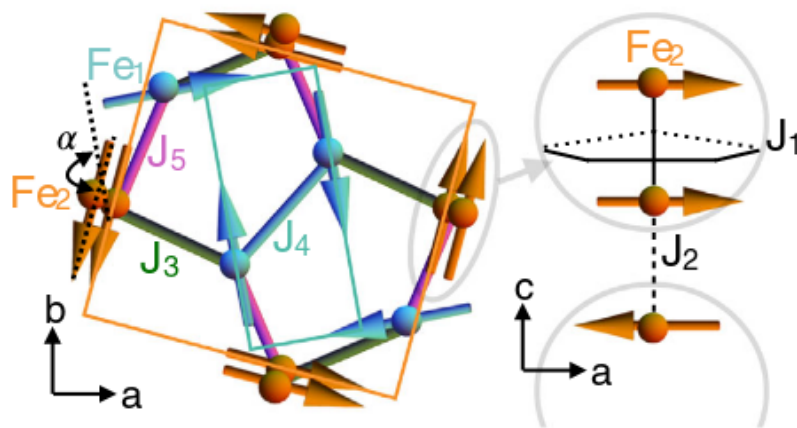
Figure 4: Magnetic ordered arrangement of Bi$_2$Fe$_4$O$_9$ as experienced below T_N. Figure from Beauvois et al. [3].

4 Neutron scattering

4.1 Neutrons

Neutrons were first detected in 1932 by Chadwick [6] and are nuclear particles with a neutral electrical charge, and a mass close to that of the proton [20],

$$m_n = 1.6749 \cdot 10^{-27} \, \text{kg}. \tag{8}$$

Important for probing magnetic phenomena, the neutron, which is a spin-$\frac{1}{2}$ particle, has a magnetic moment of

$$\mu = \gamma \mu_N \approx -9.6622 \cdot 10^{-27} \, \frac{\text{J}}{\text{T}}. \tag{9}$$

Here the neutron magnetogyric ratio is given by $\gamma = -1.9130$ and the nuclear magneton is given by $\mu_N = \frac{e\hbar}{2m_p}$. The magnetic moment, μ, couples antiparallel to the neutron spin [20].

Since the neutrons interact with nuclei through the strong nuclear force and with magnetic moments through the electromagnetic force both characteristics can be investigated by means of neutron scattering [20].

From quantum mechanics we know that particles behave both as particles and waves. This behaviour is also true for the neutron giving rise to useful phenomena e.g. Bragg diffraction. See Section 4.3.

4.2 Neutron sources

In order to do neutron scattering, one uses facilities that have a beam flux, Ψ, of 10^4 to $10^9 \, \frac{\text{n}}{\text{cm}^2\text{s}}$ at the sample position. A flux of this magnitude is achieved through one of two means: Fission or spallation [20].

In the case of fission a continuous flux is produced in a conventional fission reactor, where slow neutrons are sent into a fissile compound, e.g. ^{235}U which in return turns unstable and sends out 3 neutrons, ^{141}Ba, and ^{92}Kr [20].

Spallation on the other hand sends fast protons in the GeV-regime into a heavy nuclei exciting this and evaporating neutrons and protons in pulses [20]. One spallation source is the Swiss Spallation Neutron Source (SINQ) located at the Paul Scherrer Institute in Switzerland. Despite being a spallation source, SINQ produces a continuous neutron flux of around $10^{14} \, \frac{\text{n}}{\text{cm}^2\text{s}}$ [24]. Since not all of the 4π solid angle reaches the beam guide, this corresponds to $10^9 \, \frac{\text{n}}{\text{cm}^2\text{s}}$ at the monochromator and finally a flux of $10^7 \, \frac{\text{n}}{\text{cm}^2\text{s}}$ at the sample position (see Section 4.6.

4.3 Elastic Scattering

As mentioned previously neutrons can be treated as both particles and waves. When looking at the conditions required for scattering to happen[2], the latter is used in this treatment.

---

[2]And for scattering to be visible

The incoming and outgoing neutrons can, following this treatment, be thought of as planar waves [4],

$$\psi_j\left(\boldsymbol{r}\right) = \frac{1}{\sqrt{L^3}} e^{i\boldsymbol{k}_j \cdot \boldsymbol{r}}, \tag{10}$$

with an energy

$$E_j = \frac{\hbar^2 k_j^2}{2m_n}, \qquad \text{where } j = i, f. \tag{11}$$

A neutron in a specific state can then be described by its wave vector. From Fermi's golden rule we get the transition rate per unit time for the scattering of a particle in the initial state, $\boldsymbol{k}_i$, to the final state, $\boldsymbol{k}_f$ [5].

$$\Gamma_{i\to f} = \frac{2\pi}{\hbar} \left|\langle \boldsymbol{k}_f| V |\boldsymbol{k}_i\rangle\right|^2 \frac{\mathrm{d}n}{\mathrm{d}E_f}, \tag{12}$$

where the matrix element is

$$\langle \boldsymbol{k}_f| V |\boldsymbol{k}_i\rangle = \int \mathrm{d}\boldsymbol{r} \, \frac{e^{-i\boldsymbol{k}_f \cdot \boldsymbol{r}}}{\sqrt{L^3}} V(\boldsymbol{r}) \frac{e^{i\boldsymbol{k}_i \cdot \boldsymbol{r}}}{\sqrt{L^3}} \tag{13}$$

$$= \frac{1}{L^3} \int \mathrm{d}\boldsymbol{r} \, e^{i(\boldsymbol{k}_i - \boldsymbol{k}_f)\cdot \boldsymbol{r}} V(\boldsymbol{r}). \tag{14}$$

This, being the Fourier transform of the potential, can for a periodic potential be rewritten by introducing $\boldsymbol{r} = \boldsymbol{x} + \boldsymbol{R}$, where $\boldsymbol{R}$ is a lattice vector. Resulting in the following simplification.

$$\langle \boldsymbol{k}_f| V |\boldsymbol{k}_i\rangle = \frac{1}{L^3} \left[\sum_{\boldsymbol{R}} e^{i(\boldsymbol{k}_i - \boldsymbol{k}_f)\cdot \boldsymbol{R}}\right] \left[\int_{unit-cell} \mathrm{d}\boldsymbol{x} \, e^{i(\boldsymbol{k}_i - \boldsymbol{k}_f)\cdot \boldsymbol{x}} V(\boldsymbol{x})\right], \tag{15}$$

where L^3 is the volume of the unit-cell and thus normalizes the sum. The second term vanishes unless $\boldsymbol{q} = \boldsymbol{k}_i - \boldsymbol{k}_f$ is a reciprocal lattice vector $\boldsymbol{G}$, since $\boldsymbol{G} \cdot \boldsymbol{R} = 0$ per construction. This condition is known as the Laue condition [23].

From the geometry of Figure 5 it can be seen that

$$q^2 = k_i^2 + k_f^2 - 2k_i k_f \cos\left(2\theta\right). \tag{16}$$

Assuming that the Laue condition is satisfied, the length of $|\boldsymbol{k}_i| = |\boldsymbol{k}_f| = k = \frac{2\pi}{\lambda}$, and remembering that $|\boldsymbol{G}| = \frac{2\pi}{d}$ [23], where d is the spacing between lattice planes. We put it all together and get,

$$q^2 = 2k^2 \left(1 - \cos\left(2\theta\right)\right) \tag{17}$$

$$\implies \qquad q = 2k \sin\theta \tag{18}$$
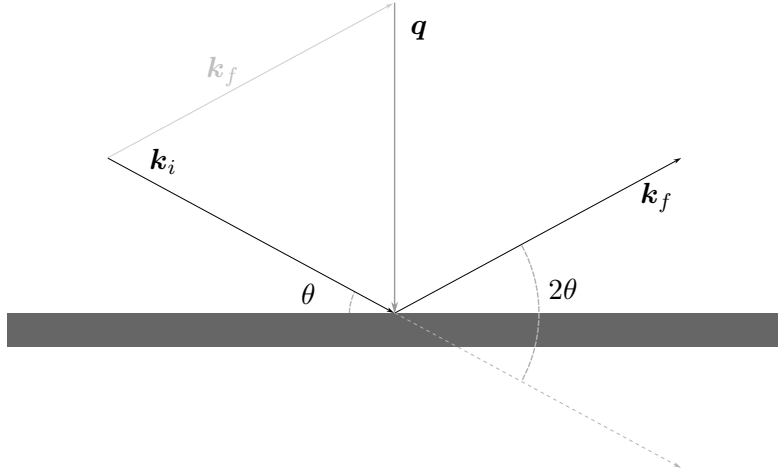
$$\implies \qquad \lambda = 2d \sin\theta. \tag{19}$$

Figure 5: The scattering vectors, $\boldsymbol{k}_i$ and $\boldsymbol{k}_f$, scattering off a plane with angles and neutron scattering vector, $\boldsymbol{q}$, shown.

This is exactly Bragg's law [23], showing that we should expect diffraction only when the angle is properly tuned to the scattering planes. Note that this is only a rule for elastic scattering since one of our assumptions were $|\boldsymbol{k}_i|^2 = |\boldsymbol{k}_f|^2$

All this comes to show that when scanning the experimental setup through different angles we will sometimes see large diffraction signal, and then we know that we have found a reciprocal lattice vector (See for example Figure 7c).

Knowing where to expect diffraction is only one part of the information that can can be obtained from scattering experiments. By looking once more at Equation (15) we see that the second term is still unused. We will call this the structure factor

$$S(\boldsymbol{q}) = \int_{unit-cell} \mathrm{d}\boldsymbol{x}\, e^{i\boldsymbol{q}\cdot\boldsymbol{x}}\, V\left(\boldsymbol{x}\right), \tag{20}$$

and see that the transition rate $\Gamma \propto |S|^2$. To get from this expression to the measured intensity, we first and foremost need to calculate the density of states and secondly look at the amount of neutrons scattered into a specific part of the crystal. Using Equation (11) we get the density of states in energy-space within a scattering direction $\mathrm{d}\Omega$ according to [20],

$$\left.\frac{\mathrm{d}n}{\mathrm{d}E_f}\right|_{\mathrm{d}\Omega} = \left.\frac{\mathrm{d}n}{\mathrm{d}V_k}\right|_{\mathrm{d}\Omega} \frac{\mathrm{d}V_k}{\mathrm{d}k_f}\left(\frac{\mathrm{d}E_f}{\mathrm{d}k_f}\right)^{-1} \tag{21}$$

$$= \frac{L^3}{(2\pi)^3}\frac{\mathrm{d}\Omega}{4\pi}4\pi k_f^2\left(\frac{2\hbar^2 k_f}{2m_n}\right)^{-1} = \frac{L^3 k_f m_n}{8\pi^3\hbar^2}\,\mathrm{d}\Omega. \tag{22}$$

Putting this into Fermi's golden rule and normalising by dividing with the flux of the source we get the scattering cross section, σ, into a small solid angle, Ω, as

$$\frac{\mathrm{d}\sigma}{\mathrm{d}\Omega} = \frac{1}{\Psi} \frac{\Gamma_{i \to f, \mathrm{d}\Omega}}{\mathrm{d}\Omega} \tag{23}$$

$$= \left(\frac{1}{L^3} \frac{\hbar k_i}{m_n} \right)^{-1} \frac{L^3 k_f m_n}{8\pi^3 \hbar^2} \tag{24}$$

$$= L^6 \frac{k_f}{k_i} \left(\frac{m_n}{2\pi \hbar^2} \right)^2 |\langle \psi_i| V |\psi_f \rangle|^2 , \tag{25}$$

where we used that the flux is equal to the speed of the neutrons multiplied with the incoming neutron density i.e. $\Psi = |\psi_i|^2 v_i$. Equation (25) is known as the master equation for scattering [20] and by applying different potentials the intensity of the scattering neutrons can be calculated. Worth noting is the factor $\frac{k_f}{k_i}$ which is unity for elastic scattering, but important for inelastic scattering.

4.3.1 Applying different potentials

Scattering of nuclei The scattering off of nuclei is due to the strong nuclear force which falls off incredibly fast allowing us to approximate the potential as a delta function. This is known as the Fermi pseudopotential [20, 23].

$$V_j(\boldsymbol{r}) = \frac{2\pi \hbar^2}{m_n} b_j \delta\left(\boldsymbol{r} - \boldsymbol{r}_j\right), \tag{26}$$

where b_j is the scattering length of the j'th nucleus located at $\boldsymbol{r}_j$, and is in general a measure of the strength of scattering from the j'th nucleus [23]. For multiple atoms, as is often the case, this can be written as a sum over j, and we thus get the structure factor

$$S\left(\boldsymbol{q}\right) = \int_{unit-cell} \mathrm{d}\boldsymbol{x} \, e^{i\boldsymbol{q}\cdot\boldsymbol{x}} \sum_j \frac{2\pi \hbar^2}{m_n} b_j \delta\left(\boldsymbol{x} - \boldsymbol{r}_j\right). \tag{27}$$

Integrating via the δ-function, this is just a sum over the atoms in the unit-cell, so

$$S\left(\boldsymbol{q}\right) = \frac{2\pi \hbar^2}{m_n} \sum_{j \in u.\text{-}c.} b_j e^{i\boldsymbol{q}\cdot\boldsymbol{x}_j} \tag{28}$$

So the matrix element becomes

$$\langle \psi_f |V| \psi_i \rangle = L^{-3} \frac{2\pi \hbar^2}{m_n} \sum_{\boldsymbol{R}} e^{i\boldsymbol{q}\cdot\boldsymbol{R}} \cdot \sum_{j \in u.\text{-}c.} e^{i\boldsymbol{q}\cdot\boldsymbol{x}_j} \tag{29}$$

Putting this into Equation (25) gives us

$$\frac{\mathrm{d}\sigma}{\mathrm{d}\Omega} = \frac{k_f}{k_i} \left| \sum_j b_j \exp(i\boldsymbol{q} \cdot \boldsymbol{r}_j) \right|^2 . \tag{30}$$

Magnetic Scattering   Magnetic scattering is governed by the nuclear Zeeman term for a neutron in the field generated by superposition of magnetic dipoles placed at each atom in the crystal. From Section 2, we combine Equations (2) and (3) to get

$$H_{Z,j} = \frac{\mu_0}{4\pi} g\mu_B \gamma\mu_N \boldsymbol{\sigma} \cdot \nabla \times \left(\frac{\boldsymbol{s}_j \times (\boldsymbol{r} - \boldsymbol{r}_j)}{|\boldsymbol{r} - \boldsymbol{r}_j|^3} \right), \tag{31}$$

where $\boldsymbol{s}_j$ is the spin of an electron at position $\boldsymbol{r}_j$, g the electronic magnetogyric ratio, and μ_B the Bohr magneton [20]. In much the same endeavour as before one can add these terms to get the full scattering potential, insert it in Equation (25) on the previous page, and after a couple of pages of vector calculus you get the master equation for magnetic scattering of unpolarised neutrons [20, eq. (3.29)]

$$\frac{\mathrm{d}\sigma}{\mathrm{d}\Omega} = (\gamma r_0)^2 \left(\frac{g}{2}\right)^2 \frac{k_f}{k_i} \sum_{\alpha,\beta} (\delta_{\alpha\beta} - \hat{q}_\alpha\hat{q}_\beta) \langle Q_\alpha(\boldsymbol{q}) \rangle \langle Q_\beta(\boldsymbol{q}) \rangle. \tag{32}$$

Here r_0 is the electronic radius, α, β run over the Cartesian coordinates, and $\langle * \rangle$ should be understood as a thermal average. $\boldsymbol{Q}$ is the Fourier transform of the spins in the lattice defined below

$$\boldsymbol{Q}(\boldsymbol{q}) = \sum_j \exp(i\boldsymbol{q} \cdot \boldsymbol{r}_j) \boldsymbol{s}_j \tag{33}$$

$$= \boldsymbol{M}(\boldsymbol{q}) F_m(\boldsymbol{q}), \tag{34}$$

where $\boldsymbol{M}$ is the magnetisation and F_m is the magnetic form factor. In the same way as for nuclear diffraction this can be expanded which leads to the multiplication of $\delta(\boldsymbol{q} - \boldsymbol{Q}_M + \boldsymbol{G})$, where $\boldsymbol{Q}_M$ is the magnetic ordering vector. This Laue condition for magnetic scattering shows as for nuclear scattering that we should expect magnetic scattering at periodic vectors $\boldsymbol{q}$.

Using the equations above we get a theoretical insight in the different scattering patterns that we measure. In this way we get some valuable information on the structure and interactions otherwise unseen.

4.4   Inelastic Scattering

In the previous section we looked at scattering in general and even shortly at Bragg's law and how it can be derived for elastic scattering. Another important part of neutron scattering is the ability to look at the dynamics of the system investigated. This can be done by examining the energy transfers between the crystal and the neutron [20]. The neutrons scatter off of the quantised vibrations or magnetic excitations (phonons and magnons respectively) and by measuring the energy transferred to the crystal at the scattering event the dispersion relations of both can be deduced [20]. The scattering from phonons is temperature-dependent through the Bose factor [20]. This dependence can be approximated through the Taylor series for $k_B T \gg \hbar\omega$, resulting in a linear dependence. This dependence scales proportionally to $|\boldsymbol{q}|^2$ for phonons. Magnons on the other hand loses intensity for high values of q as it is a magnetic scattering phenomena with the scattering cross section proportional to the magnetic form factor $F_m(\boldsymbol{q})$, which in return gets small for large q [20].

By also treating the different values of energy transfer, $E_i - E_f = \hbar\omega$, we move away from the three dimensional reciprocal space of elastic scattering and instead look at the four dimensional $(\boldsymbol{q}, \hbar\omega)$-space. This leads to a new term known as the partial differential scattering cross section

$$\frac{\mathrm{d}^2\sigma}{\mathrm{d}\Omega\,\mathrm{d}E_f}\,\mathrm{d}E_f\,. \tag{35}$$

Which for the process of scattering off a sample in an initial state $|\lambda_i\rangle$ and with the final sample state $|\lambda_f\rangle$ is (in combination with the initial and final states of the neutrons)

$$\frac{\mathrm{d}^2\sigma}{\mathrm{d}\Omega\,\mathrm{d}E_f}\bigg|_{\lambda_i \to \lambda_f} = \frac{k_f}{k_i}\left(\frac{m_n}{2\pi\hbar^2}\right)^2 L^6\,|\langle\lambda_f\boldsymbol{k}_f|\,V\,|\lambda_i\boldsymbol{k}_i\rangle|^2\,\delta\left(E_i - E_f + \hbar\omega\right). \tag{36}$$

In the case of magnetic inelastic scattering the spin of the neutron of course has to be part of the matrix element as well. We then get

$$\left(\frac{\mathrm{d}^2\sigma}{\mathrm{d}\Omega\,\mathrm{d}E_f}\right)_{magn.} \propto \sum_j e^{i\boldsymbol{q}\cdot\boldsymbol{r}_j} \int_{-\infty}^{\infty} e^{-i\omega t}\,\langle s_0\left(0\right) s_j\left(t\right)\rangle\,\mathrm{d}t\,. \tag{37}$$

Here $\langle s_0\left(0\right) s_j\left(t\right)\rangle$ is the correlation factor between two different spins at different times, as the neutron interacts with itself due to its wave nature [20].

4.5 Magnetic Critical Scattering

The temperature at which an antiferromagnet no longer experiences a sublattice magnetisation, $\boldsymbol{M}$, is known as the Néel Temperature, T_N [5]. The Néel temperature is thus the critical temperature for this transistion. For materials around a critical temperature we measure some interesting scattering effects known as critical scattering. Critical scattering in magnets, can be modelled using simple power laws [7]. To do this easily the reduced temperature is defined to be

$$t = \frac{T - T_N}{T_N}. \tag{38}$$

In this case many physical properties of the system follows the model

$$f = a\,|t|^\gamma\,, \tag{39}$$

where γ is known as the critical exponent [7]. This holds for correlation length, specific heat, magnetisation and susceptibility at temperatures close to the critical temperature. As a specific example the magnetisation follows [7]

$$M = M_0\left(-t\right)^\beta\,, \text{ for } t < 0. \tag{40}$$

4.6 CAMEA

The Continuous Angle Multi-Energy Analysis spectrometer (CAMEA) is a neutron spectrometer located at the Swiss Spallation Neutron Source (SINQ) at the Paul Scherrer Institut (PSI) in Switzerland [17].
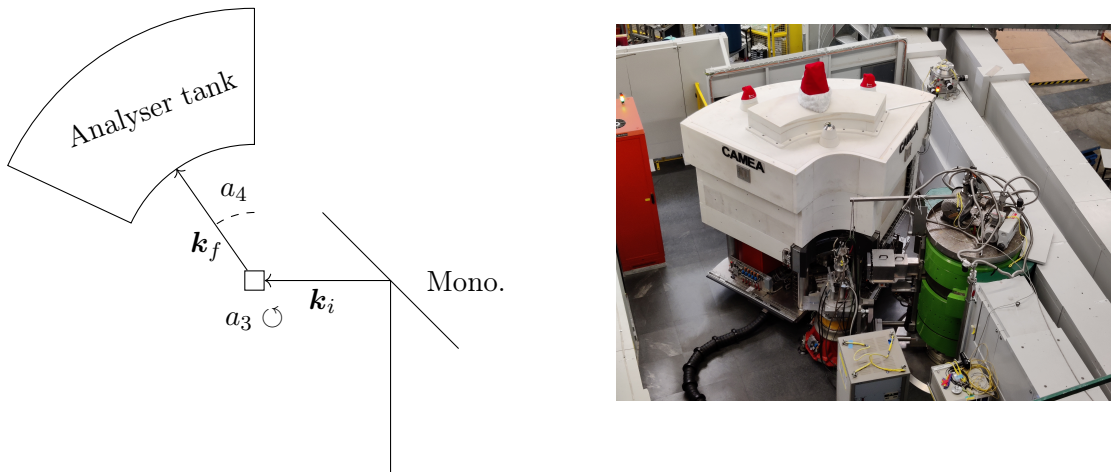
Figure 6: CAMEA at PSI. Note the different angles and vectors for the neutrons.

Neutrons are sent from SINQ into the monochromator. The monochromator at CAMEA consists of several pieces of highly ordered pyrolitic graphite [22]. By adjusting the angles of the monochromator, the beam, and the sample, only a narrow energy band, E_i, will according to Bragg's law be sent through. From here the neutrons are scattered an angle 2θ which can be varied by changing a_4 (See Figure 6). Lastly, the neutrons are sent into one of eight wedges in the detector where they scatter from one of eight pieces of pyrolitic graphite depending on their energy. This gives a range of possible measurements of E_f of 3.2–5 meV [17]. The neutrons are finally detected in one of the 13 position sensitive ^{3}He-tubes per 7.5° wedge [12]. All this gives very high resolution in both ω and $\boldsymbol{q}$.

5   Gathering of Data at CAMEA

The data for this project was collected at CAMEA at PSI in Villigen, Switzerland through two different beamtimes. One in August, and one in November of 2022. The author was present only during the latter.

In total, elastic and inelastic neutron scattering was measured at 30 different temperatures from 10 K to 800 K. Some of the measurements were done for a larger area of q-space, but all were around the rectangle bounded by $\boldsymbol{q} = (11\bar{1})$ to $\boldsymbol{q} = (221)$ as seen on Figure 7a on the following page. The data taken in August were taken for another part of q-space, but this is due to the symmetry of the system equivalent, c.f. Figures 7a and 7b.

For both beamtimes the measurements was done on a 2.35 g single crystal of $Bi_2Fe_4O_9$. Before measuring at CAMEA, the crystal was aligned along (004) and (220) at ORION [9], a two axis neutron spectrometer at PSI, in order to get the vertical alignment $\chi < 1°$. This was needed as CAMEA only has rotational degrees of freedom in the horizontal plane. The alignment was completed with $\chi_{(004)} = 0.723°$ and $\chi_{(220)} = -0.909°$. At CAMEA the monochromator was set to $E_i = 4.87$ meV and $E_i = 5$ meV. Each temperature was measured with both $a_4 = -75°$ and $a_4 = -79°$. This 4° difference is to adjust for the gaps in between the wedges and get the full picture in q-space. For each measure-

ment a_3 was scanned from 25°–115°. Afterwards, the gathered data was analysed using the Python package MJOLNIR [18], as described below.

6   Results

6.1   Q-planes

Using MJOLNIR, the first step of the data analysis was to have a look at the q-planes. To get an idea of whether the expected behaviour was visible. Two different q-planes were generated for each temperature. One elastic, $\Delta E = -0.18\,\mathrm{meV}$–$0.18\,\mathrm{meV}$, and one inelastic $\Delta E = 0.5\,\mathrm{meV}$–$2\,\mathrm{meV}$ (Though CAMEA only measures up to $1.8\,\mathrm{meV}$).
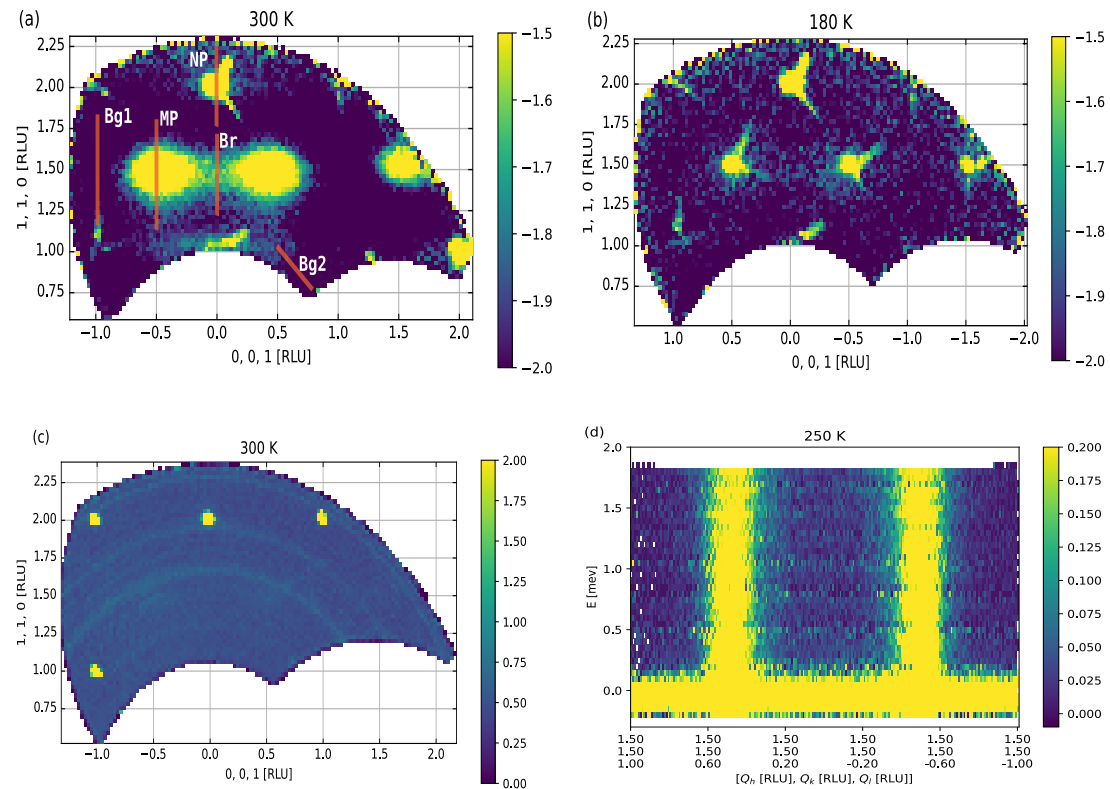
Figure 7: Two different representative maps of reciprocal space measured at $300\,\mathrm{K}$, (a), and $180\,\mathrm{K}$, (b). Integrated over the in-elastics with energy transfers from $0.5\,\mathrm{meV}$–$2\,\mathrm{meV}$. Note the different x-axes as the map at $300\,\mathrm{K}$ is measured in November and $180\,\mathrm{K}$ is measured in August. (c) shows a map of the same part of q-space as (a) but integrated over elastic energy transfers, $-0.18\,\mathrm{meV}$ to $0.18\,\mathrm{meV}$. (d) shows the relation between energy transfer and position in q-space along a cut through the magnetic peaks. Colourbars (a), (b) and (d) are on logarithmic scales to get a clearer distinction. On (a) in red is shown the approximate position of the q-cuts described in Table 2.

On the inelastic planes we see magnetic peaks at half-integer valued q-coordinates, e.g. $(1.5, 1.5, 0.5)$. This is due to the enlarged magnetic unit cell first described in Section 2. We also see some bridge in between the two magnetic peaks like the directional diffuse

scattering described by Janas et al. [14]. At the integer valued coordinates on Figure 7c, we see peaks from scattering off nuclear planes. From the inelastic q-planes we can see that though the magnetic scattering is most intense close to the critical temperature it is still present at temperatures much higher. This is also consistent with [14].

From the (q, E)-cut (Figure 7d) we can see that the inelastic magnetic peaks show no clear dispersion allowing us to integrate over large energy areas to get better statistics. These graphics make it immensely easier to make the proper cuts and find the right integration areas.

6.2   Q-cuts

After having a look at the q-planes, further investigation of some of the phenomena was done by integrating the intensity along specific lines with a width of 0.15 RLU (See Table 2), in the elastic energy range for the nuclear peaks and in all of the inelastic range for the rest.

Table 2: A brief overview of the different cuts and their MJOLNIR parameters. Where a $\pm$ is given. "+" was used for data taken in August and "−" for data from November. The MJOLNIR parameter `minPixel` was set to 0.01 for cuts with inelastic integration, and 0.02 for elastic integration. An approximate placement of the different cuts can be seen in Figure 7a.

	q_i	q_f	minPixel	width
Magnetic peak (MP)	$(2, 2, \pm 0.5)$	$(1, 1, \pm 0.5)$	0.01	0.15
Nuclear peak (NP)	$(2.1, 2.1, 0)$	$(1.9, 1.9, 0)$	0.02	0.15
Bridge (Br)	$(2, 2, 0)$	$(1, 1, 0)$	0.01	0.15
Background 1 (Bg1)	$(2, 2, \pm 1)$	$(1, 1, \pm 1)$	0.01	0.15
Background 2 (Bg2)	$(1.01, 1.01, 0.5)$	$(0.74, 0.74, 0.86)$	0.01	0.15

For each temperature the cuts shown in Table 2 where created and fitted using a constant fit for the background measurements and a Voigt profile on a linear background in the rest of the situations. The latter was chosen to combine the line width of the Gaussian instrument errors and Lorentzian scattering. The Voigt profile was implemented through the Python library SciPy [25]. An example of each of the fits can be seen in Appendix B.

In Figure 8 on the next page examples of the different cuts can be seen. Afterwards, the fitted parameters were further analysed to see if there was any structure to their development.

6.3   Error on the temperature

In the following analyses the temperature of each measurement plays an important role. The temperature measured through the experiment can be gathered through MJOLNIR and averaged for each set of measurements. A Gaussian error has been applied according to common practice, but looking at the histogram (Figure 9 on page 16) the distribution is clearly not Gaussian. This choice is suboptimal but the best of many bad alternatives.
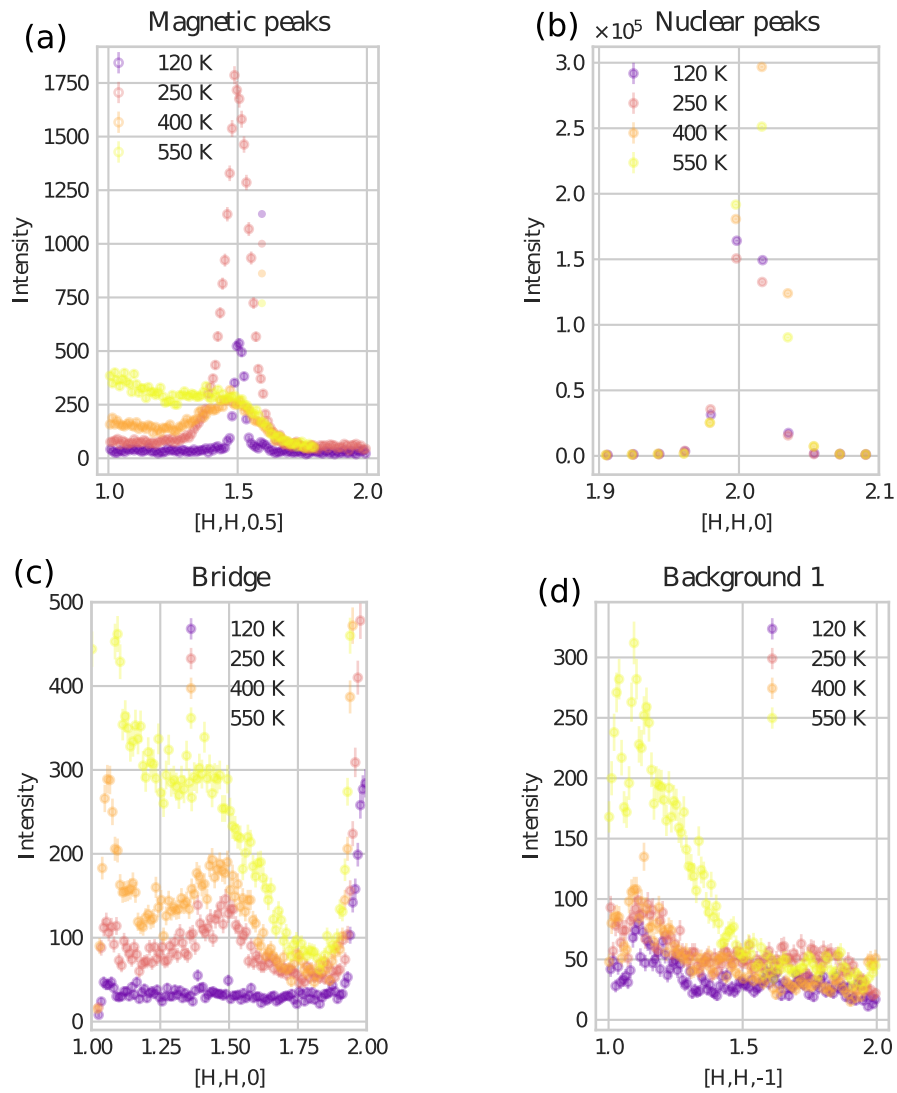
Figure 8: Examples of *q*-cuts taken at the different places in *q*-space and at different temperatures.

In the end it shouldn't make too much of a difference as the variance in T is much lower than the error on any of the fitted parameters or intensities.
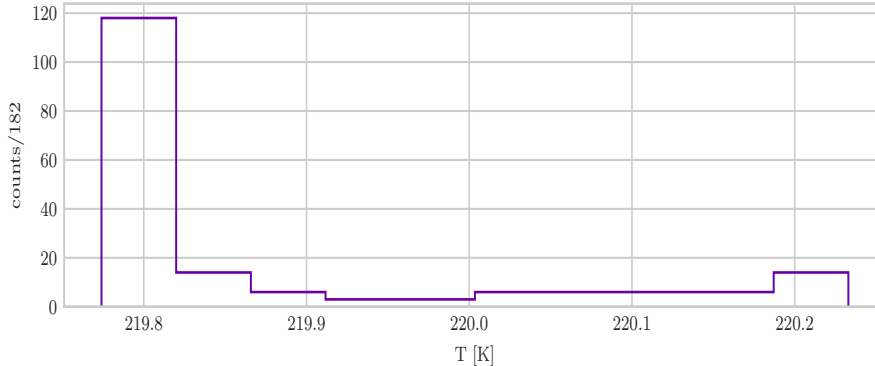

Figure 9: The different temperatures of the furnace through the measurements of $220\,\mathrm{K}$. This is representative of the other temperatures. Even though it takes this form an arithmetic mean and standard deviation has been applied to represent the different temperatures.

6.4 Background

After fitting the intensity of the background with a constant function at low temperatures,

$$\mathrm{Fit}(q) = c, \tag{41}$$

it was possible to see the linear temperature dependence as expected from the Bose factor. An interesting thing happened when looking at the temperature dependence. As seen in Figure 10 on the next page the fit at a higher q-value has a somewhat larger slope but not as large as we would have expected given that $|\boldsymbol{q}|^2$ is larger by a factor of 2.76 and the slope is only larger by a factor of 1.48. This can be due to several reasons. One that both magnons and phonons are at play and two that maybe the lower fit has some outliers at higher temperatures as they systematically lay above the fit line. Due to these rather simple results I did not go further with this investigation. The q-dependence of the background defends the choice of a linear background for the remaining fits.

6.5 Position of magnetic peaks and bridge in q-space

Looking at the q-planes, it was noticed that the magnetic peaks seemed to move closer to the origin as the temperature increased. For this reason the position of both the magnetic peak and the bridge were plotted as a function of temperature (Figure 11).

    This was done by first fitting to the nuclear Bragg peaks in the elastic q-planes, and then taking the difference between this fitted centre and the fitted centre of the magnetic peak and the bridge respectively. This was to ensure that the effect wasn't just due to the expansion of the crystal, which would lead to a contraction in all of reciprocal space.

    The fitting process was done by first fitting a Voigt profile to all q-cuts. Afterwards only the cuts where the area under the Voigt was significantly different from zero were used for the rest of the analysis. This decision was taken using a z-test (see Appendix C)
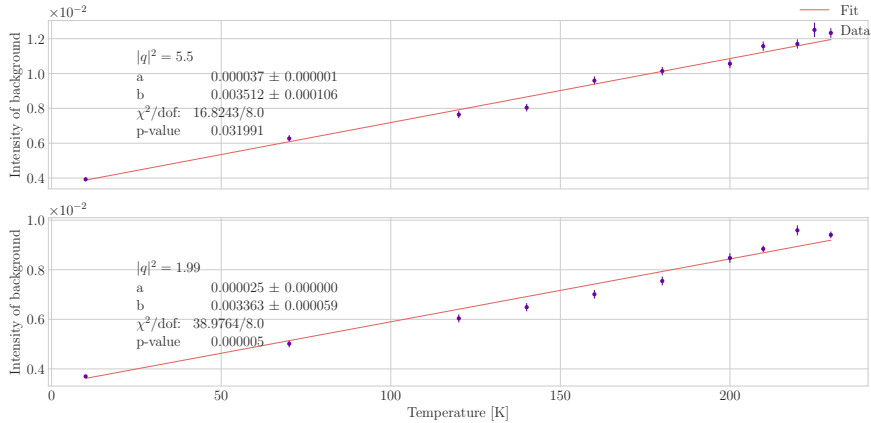
Figure 10: Linear temperature dependence of background intensity. As it can be seen the upper plot has a steeper slope than the lower.

with $z > 2$ being the cut-off limit. The bordering temperature was fitted once more with all but the amplitude kept constant using values from the approved fit. If this returned an amplitude significantly different from zero, the fit was done once more with these new starting parameters and re-evaluated. The used temperature range thus changed iteratively.

After all fitting was done the distance between each peak and the nuclear peak projected along the $(hh0)$-axis was calculated with the fitting errors propagated.
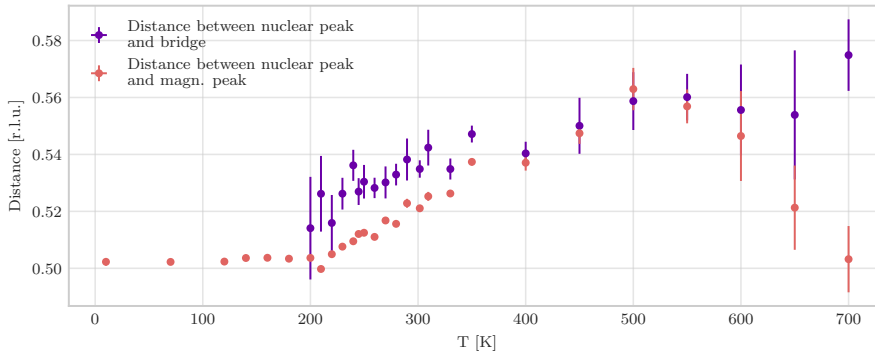

Figure 11: Movement of magnetic phenomena as a function of temperature.

6.6 Temperature dependence of magnetic peaks and bridge

The work by Janas et al. [14] (relevant figure shown in Appendix A) showed increased scattering around the Néel temperature of the frustrated system h-YMnO$_3$. It was for this reason important to also have a look at the intensity of the magnetic scattering in Bi$_2$Fe$_4$O$_9$. The integrated area under the Voigt profiles fitted to the q-cuts, with area significantly different from zero, was deemed fit as a measure of the intensity. This was plotted against temperature for both the magnetic peaks and the bridge in Figure 12.

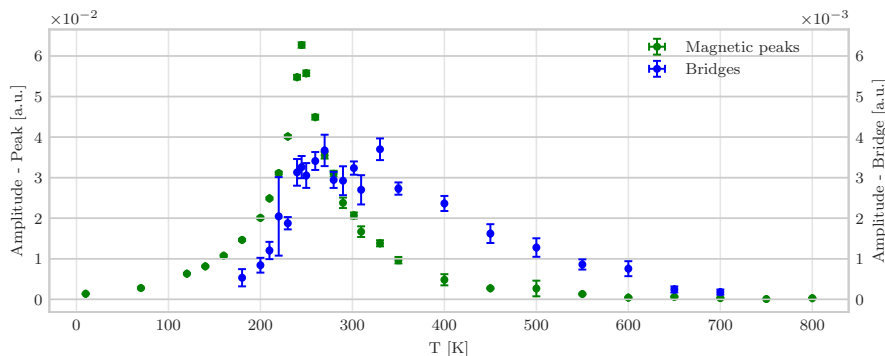Just as in the case of h-YMnO$_3$ we see a large peak for the intensity of the magnetic

Figure 12: Intensity of magnetic scattering off the bridge and magnetic peaks plotted against temperature as in Janas et al. [14]. Shown in Appendix A.

peaks just around the critical temperature, $T_C \approx 245\,\text{K}$. In accordance with Equation (39), the peak was fitted using a power law,

$$\log\left(I\right) = \gamma \cdot \log\left|1 - \frac{T}{T_C}\right| + a. \tag{42}$$

As the powerlaw only fits one side of the peak. The fitting was done iteratively by first fitting all points with $T < T_C$, for the left side, and then redoing the fit with the new fitted T_C as cut-off until all of the fitted points had $T < T_C$. For the right side of the peak the same was done with $T > T_C$ being the criteria.

Importantly the data from the beamtime in November was scaled by a constant in order to take different noise levels into account. This factor was set as a free parameter and changed to get the lowest χ^2 overall. The fits can be seen in Figure 13 on the following page. A corresponding analysis was done on the corresponding data from h-YMnO$_3$ generously supplied by Sofie Janas. This can be seen in Figure 14.

From the fits we see that T_C is significantly different for the two fits to Bi$_2$Fe$_4$O$_9$. At $T > T_C$ the fit shows $T_C = (73 \pm 4)\,\text{K}$ where $T < T_C$ shows $T_C = (296 \pm 5)\,\text{K}$. Fitting to h-YMnO$_3$, we get that the two values for T_C show no significant difference, $(58.0 \pm 1.3)\,\text{K}$ and (56.7 ± 0.5)

7   Discussion

7.1   Position of bridge

There is clear evidence for the movement of the magnetic bridge in q-space. We see from Figure 11 on the previous page that the magnetic peaks are more or less at constant coordinates up until   200 K. Hereafter the bridge is significantly present, and both signatures start moving collectively closer to origin. At high T the magnetic peaks apparently start moving back again. This can be due to either the smearing of the peak at (110), the fact that the errors on the fits at these temperatures are so large that the points aren't significantly different from the trend followed by the bridge, or a combination of the two. In some systems with helical structure it has previously been shown that a diffraction peak is able to split symmetrically around a commensurable position in q-space [15]. But since this signal moves asymmetrically, it is hardly the same
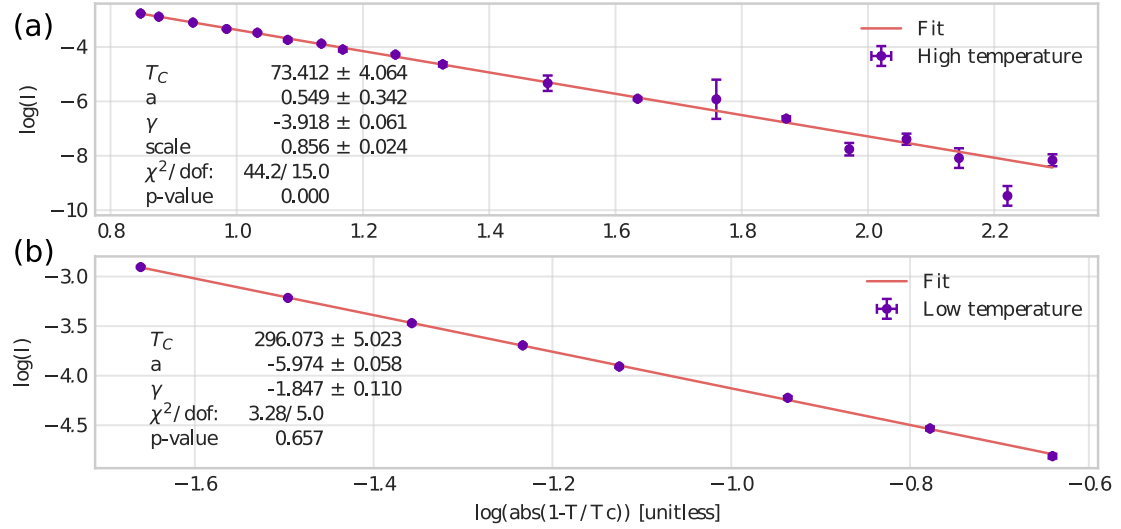
Figure 13: Powerlaw fitted to the high and low temperatures, (a) and (b) respectively. Note that the upper plot consists of data from both the November and the August beamtimes. As such the model has a scaling factor.
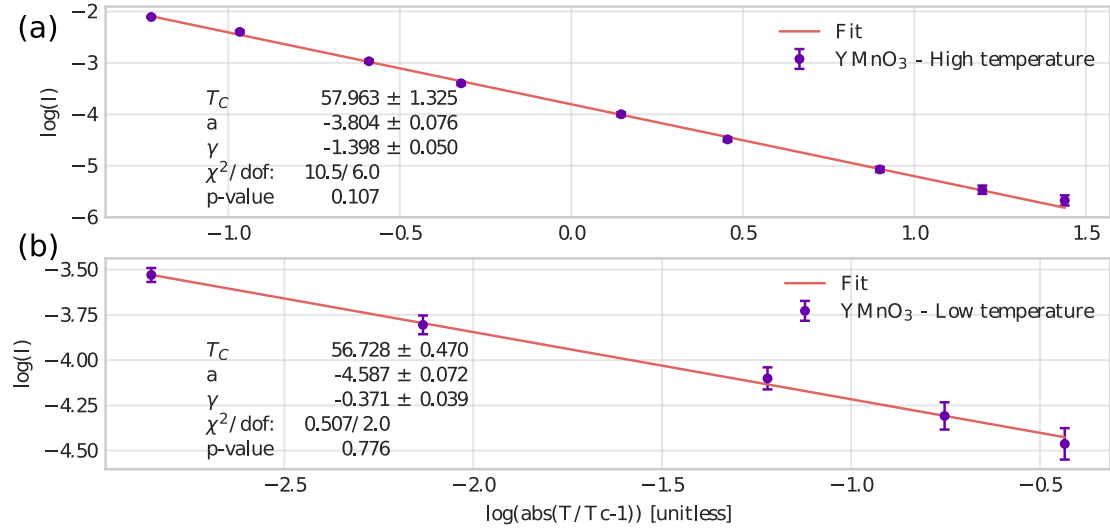

Figure 14: Powerlaw fitted to the high, (a), and low, (b), temperature data from Janas et al. [14].

in this case. Since this movement happens independently of the structural scattering it isn't an overall expansion of the crystal either.

7.2 Intensity of magnetic peak and bridge

Just as in Janas et al. [14] (see Appendix A) we see the presence of both the magnetic peaks and the diffuse bridge in-between. Furthermore, the width of the large peak in Figure 12 is much wider than what one would expect from non-frustrated systems [7]. Regarding the bridge we see scattering at temperatures much higher than T_N, when the system should be magnetically disordered. This is different from what one would expect but in accordance with the measurements of h-YMnO$_3$ [14].

All the fits seem to follow the expected power law, though the high temperature fit for Bi$_2$Fe$_4$O$_9$ (Figure 13) has $p < 0.001$, from the χ^2-test [2]. This might be due to the model only being appropriate for data sufficiently close to T_C [7]. The fitted critical temperature for Bi$_2$Fe$_4$O$_9$ is importantly significantly different for each fit ($z = 35$), but both are also far away from the expected Néel temperature. This is different from h-YMnO$_3$, where the fitted critical temperature is roughly the same, $z = 0.91$, though still far away from $T_N \approx 71$ K [14].

8 Conclusion

During this project measurements of a 2.35 g single crystal of Bi$_2$Fe$_4$O$_9$ at 12 different temperatures have been conducted, and investigated in combination with another 18 measurements done previously on the same crystal. From the data it was possible to detect magnetic peaks and a diffuse bridge as those seen in h-YMnO$_3$ [14]. Afterwards, three different behaviours were investigated, where especially two stand out. First and foremost the scattering around the critical temperature was found at significantly larger temperature ranges for different magnetic signals than what would be expected for ordinary systems. This behaviour has previously been seen in h-YMnO$_3$, another frustrated system, and one explanation might be that this happens for some frustrated magnetic systems. Secondly, a movement of the magnetic signal in q-space, starting just under T_N, was spotted with no clear explanation available.

We don't currently have the theory to describe these phenomena. As such one way to go forward could be to investigate similar systems and see if the same is true for those. This way we would be able to figure out whether this is a general behaviour of frustrated systems or if other factors plays a role. Another route would be to take a step back and look at other parts of the systems to see, if we can get a better explanation for e.g. the ordered system before going into the unordered, as much of this still isn't completely understood. Looking at the inelastic scattering in the ordered phase, we might also get a better understanding of the spin waves, which might further lead to an explanation of why we see the bridges in the unordered system.

References

[1] Chen Cheng-Yih (Joseph). "Magnetism in Chinese Culture". In: *Encyclopaedia of the History of Science, Technology, and Medicine in Non-Western Cultures*. Ed. by Helaine Selin. Dordrecht: Springer Netherlands, 2008, pp. 1263–1265. ISBN: 978-1-4020-4559-2 978-1-4020-4425-0. DOI: 10.1007/978-1-4020-4425-0_8712.

[2] Roger Barlow. *Statistics: a guide to the use of statistical methods in the physical sciences*. The Manchester physics series. Chichester, England ; New York: Wiley, 1989. 204 pp. ISBN: 978-0-471-92294-0 978-0-471-92295-7.

[3] K. Beauvois et al. "Dimer Physics in the Frustrated Cairo Pentagonal Antiferromagnet $Bi_2Fe_4O_9$". In: *Physical Review Letters* 124 (Mar. 24, 2020), p. 127202. DOI: 10.1103/PhysRevLett.124.127202.

[4] Jonas Okkels Birk. "Kritiske faseovergange i CoO nanopartikler studeret med neutronspredning". PhD thesis. Københavns Universitet, July 8, 2009. 131 pp.

[5] Stephen Blundell. *Magnetism in condensed matter*. Reprint. Oxford master series in condensed matter physics 4. Oxford: Oxford Univ. Press, 2014. 238 pp. ISBN: 978-0-19-850591-4.

[6] J. Chadwick. "Possible Existence of a Neutron". In: *Nature* 129.3252 (Feb. 27, 1932), pp. 312–312. DOI: 10.1038/129312a0.

[7] Malcolm F. Collins. *Magnetic critical scattering*. Oxford series on neutron scattering in condensed matter. New York: Oxford University Press, 1989. 188 pp. ISBN: 978-0-19-504600-7.

[8] K.L. Da Silva et al. "A local distortion of polyhedra in the novel chromium doped mullite-type bismuth ferrite $Bi_2(Cr_xFe_{1-x})_4O_9$". In: *Materials Letters* 161 (Dec. 2015), pp. 488–490. DOI: 10.1016/j.matlet.2015.09.021.

[9] *Description | ORION | Paul Scherrer Institut (PSI)*. URL: https://www.psi.ch/en/sinq/orion/description (visited on 06/13/2023).

[10] David J. Griffiths. *Introduction to electrodynamics*. Fourth edition. Cambridge, United Kingdom ; New York, NY: Cambridge University Press, 2018. ISBN: 978-1-108-42041-9.

[11] David J. Griffiths and Darrell F. Schroeter. *Introduction to quantum mechanics*. Third edition. Cambridge ; New York, NY: Cambridge University Press, 2018. 495 pp. ISBN: 978-1-107-18963-8.

[12] Felix Groitl et al. "CAMEA—A novel multiplexing analyzer for neutron spectroscopy". In: *Review of Scientific Instruments* 87.3 (Mar. 2016), p. 035109. DOI: 10.1063/1.4943208.

[13] Sofie Janas. "Neutron spectroscopy studies of geometrically frustrated antiferromagnets". PhD thesis. University of Copenhagen, Feb. 19, 2021. 189 pp.

[14] Sofie Janas et al. "Classical spin liquid or extended critical range in h-$YMnO_3$?" In: *Physical Review Letters* 126.10 (Mar. 11, 2021), p. 107203. DOI: 10.1103/PhysRevLett.126.107203. arXiv: 2006.03396[cond-mat].

[15] J. Jensen and A. R. Mackintosh. "Helifan: A new type of magnetic structure". In: *Physical Review Letters* 64.22 (May 28, 1990), pp. 2699–2702. DOI: `10.1103/PhysRevLett.64.2699`.

[16] Claudine Lacroix, Philippe Mendels, and Frédéric Mila, eds. *Introduction to Frustrated Magnetism: Materials, Experiments, Theory.* Vol. 164. Springer Series in Solid-State Sciences. Berlin, Heidelberg: Springer Berlin Heidelberg, 2011. ISBN: 978-3-642-10588-3 978-3-642-10589-0. DOI: `10.1007/978-3-642-10589-0`. URL: `https://link.springer.com/10.1007/978-3-642-10589-0` (visited on 05/30/2023).

[17] Jakob Lass et al. "Commissioning of the novel Continuous Angle Multi-energy Analysis spectrometer at the Paul Scherrer Institut". In: *Review of Scientific Instruments* 94.2 (Feb. 1, 2023), p. 023302. DOI: `10.1063/5.0128226`.

[18] Jakob Lass et al. "MJOLNIR: A software package for multiplexing neutron spectrometers". In: *SoftwareX* 12 (July 2020), p. 100600. DOI: `10.1016/j.softx.2020.100600`.

[19] Manh Duc Le et al. "Experimental determination of the magnetic interactions of frustrated Cairo pentagon lattice materials". In: *Physical Review B* 103 (Mar. 16, 2021), p. 104423. DOI: `10.1103/PhysRevB.103.104423`.

[20] Kim Lefmann. *Neutron Scattering: Theory, Instrumentation, and Simulation.* University of Copenhagen, Nov. 17, 2022.

[21] Koichi Momma and Fujio Izumi. "*VESTA 3* for three-dimensional visualization of crystal, volumetric and morphology data". In: *Journal of Applied Crystallography* 44.6 (Dec. 1, 2011), pp. 1272–1276. DOI: `10.1107/S0021889811038970`.

[22] *Parameters | CAMEA | Paul Scherrer Institut (PSI).* URL: `https://www.psi.ch/en/sinq/camea/parameters` (visited on 05/23/2023).

[23] Steven H. Simon. *The Oxford solid state basics.* 1st ed. OCLC: ocn853504907. Oxford: Oxford University Press, 2013. 290 pp. ISBN: 978-0-19-968077-1 978-0-19-968076-4.

[24] *SINQ | SINQ | Paul Scherrer Institut (PSI).* URL: `https://www.psi.ch/en/sinq` (visited on 05/18/2023).

[25] Pauli Virtanen et al. "SciPy 1.0: Fundamental Algorithms for Scientific Computing in Python". In: *Nature Methods* 17 (2020), pp. 261–272. DOI: `10.1038/s41592-019-0686-2`.

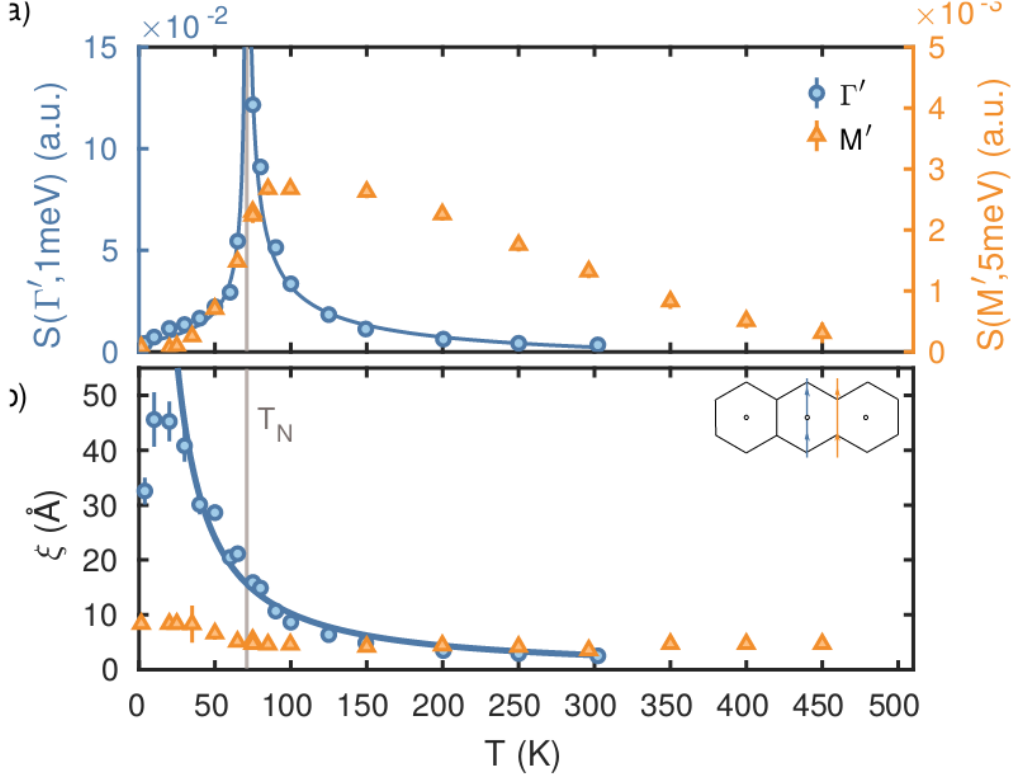# Appendix

A   Critical scattering of h-YMnO$_3$

Figure 15: *Temperature dependence of the inelastic neutron scattering data for (a) the integrated intensity and (b) the correlation length for Γ' and M'. Scan directions are shown schematically in (b). Full blue lines are power-law fits to Γ' data.* Both description and figure from [13, fig. 2a]. Γ' corresponds to the magnetic peaks descriped in this project, and M' is the bridge.

B   Fit of q-cuts

The q-cuts in this project were for the most part fitted using Voigt profiles on a linear background.

$$V(x, \sigma, \gamma) = \int_{-\infty}^{\infty} \text{Gauss}\left(x', \sigma\right) \cdot \text{Cauchy}\left(x - x', \gamma\right) dx'$$

$$\text{Fit}(x, A, \mu, \sigma, \gamma, m, c) = A \cdot V\left(x - \mu, \sigma, \gamma\right) + m \cdot x + c,$$

where Gauss and Cauchy refer to unit Gaussian and Cauchy distributions. The background was for low temperatures fitted with a constant. Examples of these fits can be seen in Figures 16 and 17. Note that these are only examples of the fits. The fit quality changes drastically when the signal disappears, and the background fit especially becomes more challenging at higher temperatures as other signals start to emerge.

(a) Magnetic peak.
$\chi^2 = 113$, $n_{dof} = 68$.

(b) Bridge.
$\chi^2 = 90$, $n_{dof} = 58$.
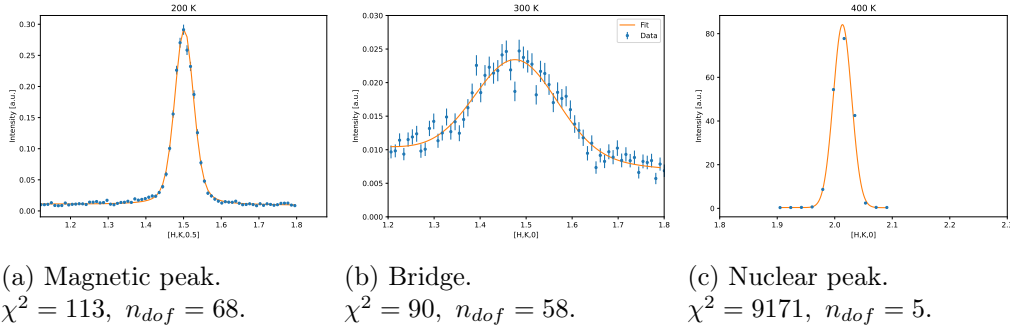
(c) Nuclear peak.
$\chi^2 = 9171$, $n_{dof} = 5$.

Figure 16: Different cuts fitted with Voigt profiles. Though the χ^2 is rather high for the nuclear peak, we see that this is probably due to the very small errors and small amount of points.
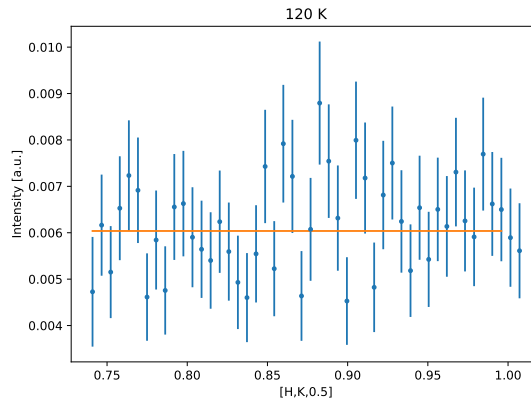

Figure 17: Constant fit to the low temperature background. ($\chi^2 = 115$, $n_{dof} = 42$).

C   *z*-test

When comparing values to each other one needs to take the error on each value into account. For this a common approach is assuming Gaussian errors and the seeing how far the values are from each other in units of the errors [2]. We define

$$z = \frac{A - B}{\sqrt{\sigma_A^2 + \sigma_B^2}}. \tag{43}$$

The *z*-test can give a *p*-value through integration of the unit Gaussian, by integrating and asking "what is the probability that I get a *z*-value of this or greater". In other words

$$p = \int_{-\infty}^{z} \frac{1}{\sqrt{2\pi}} \exp\left(-\frac{x^2}{2}\right). \tag{44}$$

Since this is dependent only on z, another approach is to chose a value for z and regard all values lower as insignificant. In this report $z = 2$ have been chosen to decide when a peak was significant which gives $p \sim 2.28\%$.

When deciding whether the area under a curve of 0.5 ± 0.03 is significantly different from zero one would calculate

$$z = \frac{0.5 - 0}{\sqrt{0.03^2 - 0^2}} = 1.67. \tag{45}$$

This is less than two and the conclusion would be that this is not significantly different from zero.

When comparing two temperatures of $(73 \pm 4)\,\mathrm{K}$ and $(296 \pm 5)\,\mathrm{K}$ one would get

$$z = \frac{296 - 73}{\sqrt{4^2 + 5^2}} = 34.83, \tag{46}$$

and conclude that they are definitely different from each other.